

Published in final edited form as:

Biomaterials. 2008 February ; 29(4): 487–496. doi:10.1016/j.biomaterials.2007.08.050.

Iron Oxide Nanoparticles as a Drug Delivery Vehicle for MRI Monitored Magnetic Targeting of Brain Tumors

Beata Chertok¹, Bradford A. Moffat², Allan E. David¹, Faquan Yu¹, Christian Bergemann³, Brian D. Ross², and Victor C. Yang^{1,4,*}

¹Department of Pharmaceutical Sciences, College of Pharmacy, University of Michigan, Ann Arbor, Michigan 48109

²Center for Molecular Imaging, Department of Radiology, School of Medicine, University of Michigan, Ann Arbor, Michigan 48109

³Chemicell GmbH, 10823 Berlin, Germany

⁴Cheung-Kong Scholar, School of Chemical Engineering, Tianjin University, Tianjin 300072, China

Abstract

This study explored the possibility of utilizing iron oxide nanoparticles as a drug delivery vehicle for minimally invasive, MRI-monitored magnetic targeting of brain tumors. *In vitro* determined hydrodynamic diameter of ~100nm, saturation magnetization of 94 emu/g Fe and T₂ relaxivity of 43 s⁻¹mM⁻¹ of the nanoparticles suggested their applicability for this purpose. *In vivo* effect of magnetic targeting on the extent and selectivity of nanoparticle accumulation in tumors of rats harboring orthotopic 9L-gliosarcomas was quantified with MRI. Animals were intravenously injected with nanoparticles (12 mg Fe/kg) under a magnetic field density of 0 T (control) or 0.4 T (experimental) applied for 30 minutes. MR images were acquired prior to administration of nanoparticles and immediately after magnetic targeting at 1 hour intervals for 4 hours. Image analysis revealed that magnetic targeting induced a 5-fold increase in the total glioma exposure to magnetic nanoparticles over non-targeted tumors (p=0.005) and a 3.6-fold enhancement in the target selectivity index of nanoparticle accumulation in glioma over the normal brain (p=0.025). In conclusion, accumulation of iron oxide nanoparticles in gliosarcomas can be significantly enhanced by magnetic targeting and successfully quantified by MR imaging. Hence, these nanoparticles appear to be a promising vehicle for glioma-targeted drug delivery.

Introduction

Malignant gliomas are one of the most debilitating and lethal forms of cancer. Despite advancement in treatments, the survival and quality of life for high-grade, malignant brain tumor patients remain poor [1]. Current treatment modalities include surgery, radiotherapy and chemotherapy [2]. Surgery and radiotherapy are hampered by the limited tumor accessibility to resection and the risk of damaging the surrounding normal tissue that may carry critical brain

© 2007 Elsevier Ltd. All rights reserved.

*Correspondence and reprint requests should be addressed to: Victor C. Yang, Ph.D, Albert B. Prescott Professor of Pharmaceutical Sciences, College of Pharmacy, University of Michigan, Ann Arbor, Michigan 48109-1065, Tel: (734) 764-4273, Fax: (734) 763-9772, vcyang@umich.edu.

Publisher's Disclaimer: This is a PDF file of an unedited manuscript that has been accepted for publication. As a service to our customers we are providing this early version of the manuscript. The manuscript will undergo copyediting, typesetting, and review of the resulting proof before it is published in its final citable form. Please note that during the production process errors may be discovered which could affect the content, and all legal disclaimers that apply to the journal pertain.

functions, whereas a major pitfall in chemotherapy is the failure to accumulate and retain a therapeutically relevant drug concentration at the tumor site [3]. Prolonged exposure of a tumor lesion to sufficiently high drug concentrations is a prerequisite for therapeutic efficacy [4]. However, passive biodistribution of a systemically administered drug, which is governed by the physicochemical properties (e.g. molecular weight, lipophilicity etc.) of the compound, often results in subtherapeutic drug levels at the tumor site [5]. Exposure of the tumor to subtherapeutic drug concentration does not only fail to irradiate the lesion, but can even stimulate overgrowth of resistant malignant cells [6]. Moreover, most chemotherapeutic agents possess poor selectivity toward the target tissue and can harm normal cells as well as cancer cells. Thus, dose escalation in order to formulate an effective dosing regimen is limited by possible systemic toxicity [4].

The failure to achieve therapeutic drug concentrations in brain tumors has been traditionally attributed to the impermeable nature of the blood brain barrier (BBB), composed of tight intercellular junctions and deficient in both pinocytotic vesicles and fenestrations [7]. Thus, strategies for circumvention or temporary disruption of the BBB, such as direct intracranial injection of chemotherapeutic drugs e.g. methotrexate [8] and drug-loaded liposomes [9], tumor implantation of BCNU-loaded polymeric wafers [10], and osmotic disruption of the BBB with hypertonic solutions of mannitol [11,12] have been attempted. However, it has been well established that glioma microvasculature exhibits physiological characteristics quite distinct from those of the intact cerebral BBB [13–16]. Structural abnormalities of the endothelial lining, driven by an erratic angiogenesis, include open endothelial gaps (interendothelial junctions and transendothelial channels), cytoplasmic vesicles and fenestrations that contribute to leakiness and hyperpermeability of the tumor vasculature [17]. Circumvention of the BBB, although it increases drug concentrations in the tumor, also inevitably results in high concentrations of the cytotoxic drug in the normal brain – posing a threat of severe neurotoxicity [18]. Similarly, direct intervention into delicate brain structures often results in the loss of neurological and neurocognitive functions [19–21]. Therefore, a reasonable approach for the design of less invasive and more selective brain tumor drug delivery is to exploit the physiological differences in vascular permeability between the tumor and normal brain to achieve potential selectivity.

Colloidal systems, such as liposomes and nanoparticles, have shown promise as drug carriers to target brain tumors after minimally invasive intravenous administration [15,22]. For example, systemic delivery of stealth liposomes loaded with the anti-cancer agent doxorubicin was found to significantly increase the extent and selectivity of drug accumulation in gliomas compared to administration of the free drug [23]. This advantage of colloidal carriers has been attributed to the so-called enhanced permeability and retention (EPR) effect [24,25], whereby macromolecules and nanoparticles, even as large as 300 nm, are able to extravasate into the tumor interstitium through the hyperpermeable vasculature of most solid tumors [15,26]. Moreover, deficient lymphatic drainage retards the tumor clearance of the macromolecular structures, rendering the use of nanoparticles a promising approach for “passive” tumor targeting.

Magnetic nanoparticles, composed of a magnetic (e.g. iron oxide/magnetite) core and a biocompatible polymeric shell (e.g. dextran, starch), offer a potential method for tumor drug delivery with benefits that extend beyond the EPR effect. These additional advantages come from such specific properties of magnetic nanoparticles as magnetic responsiveness and MRI visibility. Several investigators have previously shown that magnetic nanoparticles can be retained at tumor sites, after local administration combined with a locally applied external magnetic field, due to the “magnetic responsiveness” of the iron oxide core, thereby enabling magnetic targeting [27–30]. Additionally, it has also been demonstrated that detectable

amounts of magnetic nanoparticles are able to reach the tumor of 9L-glioma bearing rats after intravenous administration [31,32].

While colloidal carriers have been shown to accumulate in brain tumors, the assessment of accumulation and retention is often hindered by a lack of non-invasive methods to monitor the time-course of nanoparticle distribution within the brain. Since iron oxide magnetic nanoparticles are known to be strong enhancers of proton spin-spin (T_2/T_2^*) relaxation, MRI is a suitable modality for non-invasive detection of such nanoparticles [33]. The resulting reduction in signal intensity (negative contrast) at the spatial location of magnetic nanoparticles renders them visible on MR images collected *in vivo*.

In the present study, we examined the applicability of magnetic nanoparticles for both magnetically enhanced brain tumor accumulation and non-invasive MRI monitoring. We hypothesized that the fraction of magnetic nanoparticles passively reaching the brain tumor site after systemic administration would be actively retained by magnetic interaction with an externally applied magnetic field, thus prolonging tumor exposure to the drug carrier. We further hypothesized that the MRI visibility of magnetic nanoparticles could be utilized to achieve non-invasive monitoring of nanoparticle accumulation, as well as to evaluate the effect of magnetic targeting on the time-course of distribution and elimination of magnetic nanoparticles, in brain tumors.

Materials and Methods

In vitro characterization of magnetic nanoparticles

Magnetic nanoparticles (G100) were kindly provided by Chemicell® (Berlin, Germany). Total iron concentrations of nanoparticle preparations were determined by inductively coupled plasma – optical emission spectroscopy (ICP-EOS) using an Optima 2000 DV spectrometer (Perkin-Elmer, Boston MA). Samples were prepared by complete digestion of the colloidal nanoparticles in 12M hydrochloric acid (HCl) at 70°C for 2 hours. Calibration curves were constructed using standard iron solutions. Light-scattering measurements were carried out at a 90° scattering angle using Nicomp 370 submicron particle sizer (Nicomp, Santa Barbara, CA). For transmission electron microscopy (TEM) a few drops of diluted nanoparticle preparation were deposited onto carbon-coated copper grids and the grids were allowed to air-dry. TEM images were obtained using a CM-100 electron microscope (Philips Electron Optics, The Netherlands) operating at 60 kV. Magnetization measurements were performed using a MPMS-XL superconducting quantum interference device (SQUID) magnetometer (Quantum Design Inc. San Diego, CA). The freeze-dried samples of nanoparticles were analyzed at 293 K in a DC magnetic field range of 0–55 kG. The MR T_2 relaxivity (R_2) of the nanoparticles was determined using the same methods as employed in the *in vivo* experiments (as described below). For these measurements a solution of nanoparticles with an iron concentration of 0.179 mM was used.

Animal model

Cell culture—Rat 9L-glioma cells (Brain Tumor Research Center, University of California, San Francisco) were cultured in Dulbecco's modified Eagle's medium (DMEM) supplemented with 10% heat-inactivated fetal bovine serum, 100 IU/mL penicillin, 100 µg/mL streptomycin and 0.29 mg of L-glutamine at 37°C in a humidified atmosphere of 5% CO₂. Prior to implantation, cells were grown to confluency in 100 mm culture dishes and harvested using 0.25% trypsin/0.1% ethylene-diamine-tetra-acetic acid (EDTA) solution. Cells were pelleted by centrifugation at 1000 × g for 5 min, resuspended in serum free DMEM at a concentration of ~10⁵ cells/µL and kept on ice until use.

Induction of brain tumors—All animal experiments were conducted according to the protocols approved by the University of Michigan Committee on Use and Care of Animals (UCUCA).

Intracerebral 9L tumor induction was carried out as previously reported [34]. Male Fisher 344 rats (125–150 g, Harlan Sprague Dawley Inc., Indianapolis, IN) were anesthetized by intraperitoneal injection of ketamine/xylazine mixture (87/13 mg/kg body weight). A small skin incision was made over the right hemisphere and the tissue was carefully removed until the bregma was identified. A 1-mm-diameter burr hole was drilled through the skull 1 mm anterior to the bregma and approximately 5 mm lateral from the midline. Ten microliters of 9L cell suspension was injected through the burr hole at a depth of 3 mm beneath the skull. The surgical field was cleaned with 70% ethanol and the burr hole was filled with bone wax (Ethicon Inc., Summerfield, NJ) to prevent extracerebral extension of the tumor and the skin incision was closed with tissue adhesive (3M Vetbond, Animal Care products, St Paul, MN). Animals were imaged using MRI beginning at 10 days post-cell implantation to select tumors between 50 and 70 μL in volume as previously described [34].

Magnetic targeting

G100 nanoparticle suspensions were diluted with PBS and filtered through a 0.2 μm disposable syringe filter to obtain a preparation of about 6 mg Fe/mL, as determined by ICP-EOS described above. Animals were anesthetized with an inhaled mixture of 1.5 % isoflurane/air and tail veins cannulated using a 26-gauge angiocatheter (Angiocath™, Becton Dickinson, Sandy, UT). The animals were then placed ventrally on a platform with their head positioned between the poles of an electromagnet. The magnetic field density within the air gap between the poles was adjusted to 0 T (control) or 0.4 T (experimental). Animals were then injected with nanoparticle suspension at a dose of 12 mg Fe/kg through the catheter and retained in the magnetic field for 30 min.

MR imaging

MRI was performed using a 12-cm horizontal-bore, 7 Tesla Varian Unity Inova imaging system (Varian, Palo Alto, CA). Animals were anesthetized with 1.5 % isoflurane/air mixture and maintained at 37°C inside the magnet. The heads of the animals were positioned in the center of a 35-mm-diameter quadrature RF volume coil (USA Instruments Inc, OH). A single-slice gradient echo sagittal image was acquired to facilitate reproducible positioning of the animal head within the coil using the base of the skull as a reference point. The time course of nanoparticle distribution in the rat brain was monitored by serial acquisition of gradient echo (GE) and T_2 -weighted MRI scans. Images were acquired before administration of nanoparticles (pre-scans) and after magnetic targeting at approximately 45 min intervals over a 4 hour period.

All images were acquired with a field of view (FOV) of 30 \times 30 mm over 128 \times 128 matrix. Since animals had to be repositioned within the magnet, quantitative information on nanoparticle accumulation was inferred by measuring R_2 relaxivity. T_2 -weighted images were acquired using a multi-slice fast spin echo sequence. At each time point (t) of MRI data acquisition, two consecutive sets of 13 axial 1-mm-thick slices of the brain were collected with effective echo time (TE) fixed to either 30 or 60 ms. Relaxation time (TR) was set to 4 sec and four signal averages were collected per phase encoding step. R_2 relaxivity maps were calculated from signal intensities using the following equation:

$$R_2(t) = \frac{1}{T_2(t)} = \frac{\ln[S_1(TE_1, t)/S_2(TE_2, t)]}{TE_2 - TE_1} \quad [1]$$

where $S_1(TE_1, t)$ and $S_2(TE_2, t)$ are the signal intensities at time (t) following the administration of nanoparticles acquired with effective echo times TE_1 and TE_2 , respectively.

The 13 sections of the rat brain collected with the T_2 -weighted spin echo MRI were used to determine the position of the slice having best cross-sectional visualization of the tumor lesion. Gradient Echo single slice scan was acquired at this position to provide qualitative information on nanoparticle accumulation in the tumor. The image was produced with $TR=20$ msec, $TE=5$ msec and a slice thickness of 1 mm.

Quantitative analysis of MRI data

The R_2 values used to analyze the time course of R_2 relaxivity change after nanoparticle administration were obtained from the mean signal intensity within defined regions of interest (ROIs) on the R_2 relaxivity maps. The ROIs were manually drawn in the tumor lesion and contra-lateral normal brain. The change in R_2 relaxivity caused by the presence of the contrast agent within the tissue of interest at time t was expressed as a percentage change of the initial (pre-scan; $t=0$) relaxivity value:

$$dR_2(\%) = \frac{R_2(t) - R_2(0)}{R_2(0)} \times 100\% \quad [2]$$

To compare the overall exposure of the glioma and contra-lateral normal brain tissue to magnetic nanoparticles with and without magnetic targeting, the area under the curve (AUC) of dR_2 versus time was calculated. The AUC was estimated numerically by a linear trapezoidal integration method; integration interval was chosen to be 45–260 min after nanoparticles administration, corresponding to the time period of data collection.

The selectivity of nanoparticle accumulation in tumor versus contra-lateral normal brain was determined by calculating the target selectivity index (TSI). TSI was defined as follows:

$$TSI = \frac{AUC_{(45-260 \text{ min})}(\text{glioma})}{AUC_{(45-260 \text{ min})}(\text{contra - lateral brain})} \quad [3]$$

Ex vivo Electron Spin Resonance (ESR) analysis of nanoparticle concentrations

Excised tissues of targeted and non-targeted animals were analyzed for nanoparticle content by ESR spectroscopy. In these studies, rats (experimental: $n=6$, control: $n=6$) were subjected to magnetic targeting and 50 min after the administration of magnetic nanoparticles pre-anesthetized animals were sacrificed. The brain was immediately removed and divided into right and left hemispheres. The tumor was carefully dissected from the normal tissue of the right hemisphere. The left hemisphere and the tumor tissues were frozen on dry ice and kept at -80°C .

Nanoparticle concentrations in tissue samples were determined by a modified method of Mykhaylyk et al. [11]. Briefly, ESR spectra of weighted tissue samples and standard nanoparticle solutions were acquired using an EMX ESR spectrometer (Bruker Instruments Inc., Billerica, MA) equipped with a liquid nitrogen cryostat. The acquisition parameters were: resonant frequency: $\sim 9.2\text{GHz}$, microwave power: 20mW, temperature: 145K, modulation amplitude: 5G and receiver gain: 5×10^4 . The ESR signal was collected as the first derivative of the absorption of microwave power and plotted versus the magnitude of the applied magnetic field. For quantitative purposes, a double integration was applied to obtain the AUC for the absorption-field curve; data were corrected for background tissue absorption of the microwave

radiation using tissue samples of glioma-bearing rats not exposed to magnetic nanoparticles. A calibration curve was constructed by plotting integral intensities of the ESR spectra of standard nanoparticle solutions versus their known iron concentrations, as determined by ICP-EOS. The calibration curve was linear ($R^2=0.99$) within the range of 0.1–9 nmol Fe.

Statistical analysis

Data are presented as mean \pm SE, unless indicated otherwise. Nanoparticle accumulation and target selectivity index in targeted and non-targeted groups were compared using the unpaired *t* test. A *p*-value of <0.05 was considered statistically significant. Tumor elimination profiles of nanoparticles in the non-targeted group was fitted to a monoexponential function with Curve Fitting Toolbox of Matlab 7.1 software (The MathWorks, MA) using the nonlinear least squares regression method with Levenberg-Marquardt algorithm. Regression analysis of the ESR versus MRI data sets were carried out using the linear least squares algorithm (Excel, Microsoft, CA).

Results

In vitro characterization of magnetic nanoparticles

According to previous investigations [35], the success of magnetic targeting is generally contingent upon the magnetic properties and size distribution of the nanoparticles. In addition, the ability of the nanoparticles to enhance proton relaxation is a pre-requisite for their MRI visibility [36]. The G100 nanoparticles consisted of an iron oxide core and a starch coating (Figure 1A), and exhibited a narrow distribution of the hydrodynamic diameter of 110 \pm 22 nm (mean \pm SD) (Figure 1B). The iron oxide core consisted of multiple separate crystals as displayed by a TEM image of a typical single nanoparticle (Figure 1C). The nanoparticle magnetization, induced by an applied magnetic field, increased with increasing applied field strength and reached a saturation magnetization (M_s) value of 94 emu/g Fe (Figure 1D). The magnetization curve displayed negligible hysteresis, indicating superparamagnetic behavior of the sample (Figure 1D, inset). In fact, superparamagnetism can be of great advantage in tumor targeting since superparamagnetic nanoparticles possess zero net magnetic moment in the absence of an external magnetic field and therefore yield minimal self-aggregation tendency outside of the targeted region [33]. The R_2 relaxivity value of the G100 nanoparticles was found to be 43.8 \pm 2.6 s⁻¹mM⁻¹ (mean \pm SD). This relaxivity is comparable to the R_2 of the clinically relevant MR contrast agent Combidex® (Advanced Magnetics, MA, $R_2=53.1 \pm 3.3$ s⁻¹mM⁻¹ [37]).

In vivo Magnetic targeting

Figure 2 presents a subset of a typical series of MRI images obtained from targeted and non-targeted animals before and after nanoparticle administration. The brain tumors are clearly visible on the baseline T_2 -weighted images (Figures 2A and 2B). The GE images of the targeted animal acquired 1 and 3 hours post injection (0.5 and 2.5 hours post magnetic targeting, respectively) exhibited a region of pronounced hypointensity compared to the baseline GE image (Figure 2A). This hypointense region indicated the presence of magnetic nanoparticles within the tumor tissue. In contrast, the post-injection images of the non-targeted animal (Figure 2B) showed almost no signal reduction within the glioma lesion. These results qualitatively demonstrated that magnetic targeting improved glioma accumulation and retention of the magnetic nanoparticles.

GE images, however, incorporate main magnetic field inhomogeneities, the spatial distribution of which may vary with repositioning of the animal inside the magnet. Animal repositioning between the scans at different time points was essential due to the interval of magnetic targeting and long overall time frame of the kinetic monitoring. Therefore, quantitative information on

nanoparticle brain distribution was inferred from R_2 relaxivity maps for targeted (Figure 3A) and control (Figure 3C) animals with the assumption that the change in relaxivity, relative to the pre-scan (dR_2), was dominated by the change in nanoparticle concentration.

The kinetic pattern of dR_2 variation within the ROIs of glioma and contra-lateral normal brain in both targeted (Figure 3B) and control (Figure 3D) animals showed that magnetic targeting profoundly altered the kinetic profile of nanoparticle accumulation within the tumor lesions. In non-targeted animals the kinetic process observed within the tumor region during the data collection interval (45–260 min post-injection) could be described as a typical first-order mono-exponential elimination (decay rate: $b=-1.17 \text{ min}^{-1}$, $R^2=0.97$, $\text{RMSE}=0.55$) (Figure 4A). In contrast, the glioma disposition curve for the targeted animals could not be accurately fitted by a monoexponential function ($R^2=0.51$), indicating a more complicated disposition process. The AUC analysis (Figure 4B) showed that overall tumor exposure to magnetic nanoparticles was 5-fold greater ($p=0.005$) for the targeted animals ($2,528 \pm 395 \text{ \%*min}$, $n=5$) compared to the control group ($477 \pm 33 \text{ \%*min}$, $n=5$).

Another prominent phenomenon observed in Figures 3 was that the pronounced increase in glioma exposure to nanoparticles due to magnetic targeting was not accompanied by a corresponding increase of nanoparticle accumulation in the contra-lateral normal brain. The selectivity of nanoparticle accumulation in gliosarcoma over normal brain was significantly enhanced ($p=0.025$) by magnetic targeting, as reflected by the 3.6-fold increase in target selectivity index obtained for the targeted group (11.9 ± 3.3 , $n=5$) versus the control group (3.3 ± 1.1 , $n=5$) (Figure 4C).

Ex vivo ESR tissue analysis

To validate the non-invasive, MRI-based nanoparticle quantification technique, nanoparticle concentrations in the excised tissue samples of glioma and normal brain were also estimated using ESR spectroscopy. As shown in Figure 5A, the tumor tissue excised from a targeted animal (Spectrum #2 in Figure 5A) exhibited the same ESR spectrum as that of the calibration solution containing G100 magnetic nanoparticles (Spectrum #1 in Figure 5A). The lack of an ESR signal from glioma tissue of rat not exposed to the magnetic nanoparticles (Spectrum #3 in Figure 5A) further confirms that the signal measured in the targeted tumor tissue could be primarily attributed to the presence of the magnetic nanoparticles.

Quantitative analysis of the ESR spectra (Figure 5B) demonstrated that the nanoparticle concentration in tumor tissues obtained from targeted animals 50 min after injection was 11.5-fold higher ($p<0.0005$) than that of control animals (29.8 ± 7.9 versus $2.6 \pm 0.7 \text{ nmol Fe/g}$ tissue, for the targeted and control groups, respectively, $n=6$ in each animal group). A 9.5-fold difference ($p<0.0005$) in the nanoparticle concentration was also observed between the targeted tumor tissue ($29.8 \pm 7.9 \text{ nmol Fe/g}$ tissue, $n=6$) and contra-lateral normal brain tissue ($3.1 \pm 2.1 \text{ nmol Fe/g}$ tissue, $n=6$) of the animals exposed to the magnetic field. Moreover, the ESR data obtained from the excised tumors were found to be linearly correlated (slope= $0.57 \text{ g tissue/nmol Fe}$, $p=0.0001$, $R^2=0.88$) with the dR_2 results (Figure 5C).

Discussion

Established differences in the vascular architecture and permeability of brain tumors and uncompromised normal brain tissues offer an attractive physiological basis to achieve tumor-selective accumulation of drug carriers [15,17]. In addition to selectivity, residence time of the carrier at the tumor site is of critical importance since it determines the total extent of exposure of the tumor mass to the potential drug. A major goal of the present study was to assess whether magnetic interaction between magnetic nanoparticles and a locally applied external magnetic field could affect accumulation selectivity and retention of the nanoparticles at the brain tumor

site after systemic administration. Since retention is a kinetic parameter, evaluation of the time-course of nanoparticle disposition in the brain is essential.

Concentrations of magnetic nanoparticles in both tumor and normal brain tissues have previously been quantified by methods involving tumor excision and nanoparticle extraction [38]. These methods, aside from being invasive, are also hampered by high intersubject variability, thereby impeding interpretation of the kinetic profiles of nanoparticle disposition. Therefore, an additional goal of this study was to develop a relatively simple MRI-based method for non-invasive monitoring of magnetic nanoparticle brain disposition. Previous studies have demonstrated that the change in R_2 relaxivity is related to the tissue concentration of contrast agent [39–41]. We hypothesized that factors, other than nanoparticle concentration, that could affect R_2 (e.g. blood volume, tumor oxygenation, vascular density) would exhibit negligible fluctuation during the course of our experiments. To this regard, our method was based on estimation of R_2 relaxivity as a measure of nanoparticle concentration. The validity of this method was confirmed by the independent *ex vivo* ESR analysis of nanoparticle concentrations (Figure 5).

The robustness of R_2 relaxivity as a parameter reflective of nanoparticle concentration stems from the fact that R_2 relaxivity is independent of the effects of animal repositioning inside the MRI magnet. This is because the SE based pulse sequence fully refocuses spin dephasing induced by static field inhomogeneities of the main magnetic field, thus offsetting the variability in field inhomogeneities distribution with animal repositioning. The total acquisition time for relaxivity estimation was only about 8 minutes, permitting sufficiently frequent sampling of the time-course of nanoparticle disposition.

The time-course of dR_2 within the gliosarcoma lesion of the magnetically targeted animals was pronouncedly distinct from the control animals, suggesting the glioma retention effect of magnetic nanoparticles induced by the presence of an external magnetic field (Figure 3). In control animals, the glioma elimination of magnetic nanoparticles could be described by monoexponential decay (Figure 4A). This is characteristic of a single-compartment elimination profile suggesting an intravascular confinement of glioma-reaching magnetic nanoparticles in the absence of external magnetic field. This observation also revealed a minimal contribution of the EPR effect to glioma retention of magnetic nanoparticles. Low selectivity of nanoparticle accumulation in the gliosarcoma over the normal brain in control animals, despite the pronounced differences in vascular permeability between the intact blood-brain barrier and the compromised blood-tumor barrier, was an interesting finding of this study. A possible explanation for that would be a low rate of nanoparticle extravasation compared to their residence time in the tumor vasculature. However, further studies are required to confirm this hypothesis.

Nevertheless, an important finding of the present study was that in magnetically targeted animals the glioma retention of nanoparticles persisted for approximately 100 minutes after the removal of the external magnetic field. Susceptibility-based MRI signal reduction within the glioma lesion due to the presence of magnetic nanoparticles cannot be used to discriminate between extensive perfusion of glioma lesion and interstitial glioma accumulation of the nanoparticles. However, the observation of about 11.5-fold higher nanoparticle concentrations in excised glioma tissues of magnetically targeted animals over the control group strongly suggested tumor entrapment of magnetic nanoparticles facilitated by the magnetic field (Figure 5B). Possibly, the magnetic field gradient acts to oppose the hemodynamics and mediates retention of magnetic nanoparticles within tumor vasculature thus increasing the chances of the nanoparticles to extravasate. Other researchers have demonstrated that magnetized nanoparticles aggregate inside tumor interstitium and the aggregates remain entrapped within the interstitial matrix [38]. When the magnetic field is discontinued, the aggregation might be

slowly reversed due to magnetic relaxation of the superparamagnetic nuclei, allowing the nanoparticles to clear from the glioma lesion. This previously proposed mechanism offers a plausible explanation for the 4-fold increase in glioma accumulation selectivity induced by magnetic targeting. However, confirmation of this mechanism of nanoparticle retention within glioma requires further investigation.

Although the accumulation of nanoparticles was quantified indirectly by measurement of the dR_2 changes *in vivo* using MRI, it was confirmed by direct measurement of nanoparticle concentrations *ex vivo* (Figure 5). ESR spectroscopy was the method of choice for the *ex vivo* analysis. MRI and ESR techniques are both based on the phenomenon of magnetic resonance; however MRI is only able to indirectly detect the presence of magnetic nanoparticles via their effect on the water proton relaxation process. In contrast, ESR directly measures the presence of paramagnetic species. Determination of the nanoparticles within the tumor by ESR therefore served as a robust validation of the non-invasive MRI technique for nanoparticle quantification.

The feasibility of utilizing magnetic nanoparticles as a platform for delivery of drugs to brain tumors would depend on the toxicity, the route of administration and the accumulation selectivity (i.e. towards the glioma over the uncompromised normal brain) of the nanoparticles, as well as the desorption kinetics of the drug from the carrier. Although magnetically mediated glioma targeting of magnetic nanoparticles has been previously demonstrated [38], the nanoparticles were administered via the carotid artery involving permanent ligation of the common carotid, external carotid, occipital and pterygopalatine arteries. In contrast, in the present study the nanoparticles were administered intravenously. This minimally invasive approach, which is not hindered by problematic post-surgical animal recovery, provides a straightforward and clinically relevant method to investigate multiple-dose therapeutic regimens of drug delivery to brain tumors via magnetic nanoparticle targeting. The magnetic nanoparticles used in the current study have already been reported by other investigators to be non-toxic and well tolerated in both preclinical and clinical trials after systemic administration, even at doses 10-times higher than those employed in our experiments [42,43]. In addition, previous studies have demonstrated the feasibility of loading drugs onto magnetic nanoparticles and examined the kinetics of drug desorption. For example, it has been shown that a nanoparticle-bound chemotherapeutic agent mitoxantrone could be completely released from the carrier within 60 minutes [44]. Based on this release kinetics, the nanoparticle retention time within the tumor tissue (about 150 minutes) achieved in the present study (Figure 3C) seems to be sufficiently long for unloading the therapeutic cargo.

Conclusions

Results presented reveal that continued development of magnetic nanoparticle based systems for the delivery of chemotherapeutic agents to brain tumors is warranted. Intravenous administration, along with magnetic targeting resulted in a 5-fold increase in the total glioma exposure to magnetic nanoparticles over non-targeted tumors and a 3.6-fold enhancement in the target selectivity index of nanoparticle accumulation in glioma tissue over normal brain parenchyma. In addition, the ability to monitor magnetic nanoparticle distribution *in vivo* using clinically translatable MRI methods developed in this study offers a major advantage to non-invasively validate the localization of the drug delivery vehicle at the respective target site.

Acknowledgments

The authors would like to thank Dr. Kyle Kuszpit for his help with animal surgery. This study was partially supported by NIH Grants RO1 HL55461, RO1CA114612, R24 CA083099 and the Hartwell Foundation Biomedical Research Grant. Fred W. Lyons Jr. Fellowship and Rackham Predoctoral Award for Beata Chertok are gratefully acknowledged.

References

1. Fisher PG, Buffler PA. Malignant Gliomas in 2005: Where to GO From Here? *JAMA* 2005;293(5): 615–617. [PubMed: 15687318]
2. Newton HB. Primary brain tumors: review of etiology, diagnosis and treatment. *American Family Physician* 1994;49(4):787–797. [PubMed: 8116514]
3. Zhou R, Mazurchuk R, Straubinger RM. Antivasculature effects of doxorubicin-containing liposomes in an intracranial rat brain tumor model. *Cancer Res* 2002;62(9):2561–2566. [PubMed: 11980650]
4. Gutman RL, Peacock G, Lu DR. Targeted drug delivery for brain cancer treatment. *Journal of Controlled Release* 2000;65:31–41. [PubMed: 10699267]
5. Motl S, Zhuang Y, Waters CM, Stewart CF. Pharmacokinetic considerations in the treatment of CNS tumours. *Clin Pharmacokinet* 2006;45(9):871–903. [PubMed: 16928151]
6. Heimberger AB, Archer GE, McLendon RE, Hulette C, Friedman AH, Friedman HS, et al. Temozolomide delivered by intracerebral microinfusion is safe and efficacious against malignant gliomas in rats. *Clin Cancer Res* 2000;6(10):4148–4153. [PubMed: 11051269]
7. Lesniak MS, Brem H. Targeted therapy for brain tumours. *Nat Rev Drug Discov* 2004;3(6):499–508. [PubMed: 15173839]
8. Tator CH, Wassenaar W. Intraneoplastic injection of methotrexate for experimental brain-tumor chemotherapy. *J Neurosurg* 1977;46(2):165–174. [PubMed: 833633]
9. Saito R, Bringas JR, McKnight TR, Wendland MF, Mamot C, Drummond DC, et al. Distribution of liposomes into brain and rat brain tumor models by convection-enhanced delivery monitored with magnetic resonance imaging. *Cancer Res* 2004;64(7):2572–2579. [PubMed: 15059914]
10. Tamargo RJ, Myseros JS, Epstein JI, Yang MB, Chasin M, Brem H. Interstitial chemotherapy of the 9L gliosarcoma: controlled release polymers for drug delivery in the brain. *Cancer Res* 1993;53(2): 329–333. [PubMed: 8417826]
11. Mykhaylyk O, Cherchenko A, Ilkin A, Dudchenko N, Ruditsa V, Novoseletz M, et al. Glial brain tumor targeting of magnetite nanoparticles in rats. *Journal Of Magnetism And Magnetic Materials* 2001;225(1–2):241–247.
12. Neuwelt EA, Rapoport SI. Modification of the blood-brain barrier in the chemotherapy of malignant brain tumors. *Fed Proc* 1984;43(2):214–219. [PubMed: 6692941]
13. van der Sanden BP, Rozijn TH, Rijken PF, Peters HP, Heerschap A, van der Kogel AJ, et al. Noninvasive assessment of the functional neovasculature in 9L-glioma growing in rat brain by dynamic IH magnetic resonance imaging of gadolinium uptake. *J Cereb Blood Flow Metab* 2000;20(5):861–870. [PubMed: 10826537]
14. Boyle FM, Eller SL, Grossman SA. Penetration of intra-arterially administered vincristine in experimental brain tumor. *Neuro-oncol* 2004;6(4):300–305. [PubMed: 15494097]
15. Sharma US, Sharma A, Chau RI, Straubinger RM. Liposome-mediated therapy of intracranial brain tumors in a rat model. *Pharm Res* 1997;14(8):992–998. [PubMed: 9279878]
16. Wiranowska M, Gonzalvo AA, Saporta S, Gonzalez OR, Prockop LD. Evaluation of blood-brain barrier permeability and the effect of interferon in mouse glioma model. *J Neurooncol* 1992;14(3): 225–236. [PubMed: 1281226]
17. Vajkoczy P, Menger MD. Vascular microenvironment in gliomas. *J Neurooncol* 2000;50(1–2):99–108. [PubMed: 11245285]
18. Neuwelt EA, Glasberg M, Frenkel E, Barnett P. Neurotoxicity of chemotherapeutic agents after blood-brain barrier modification: neuropathological studies. *Ann Neurol* 1983;14(3):316–324. [PubMed: 6195955]
19. Packer RJ. Brain tumors in children. *Archives of neurology* 1999;56:421–425. [PubMed: 10199329]
20. Weitzner MA, Meyers CA. Cognitive functioning and quality of life in malignant glioma patients: a review of the literature. *Psychooncology* 1997;6(3):169–177. [PubMed: 9313282]
21. Chiras J, Dormont D, Fauchon F, Debussche C, Bories J. Intra-arterial chemotherapy of malignant gliomas. *Journal of Neuroradiology* 1988;15:31–48.
22. Gulyaev AE, Gelperina SE, Skidan IN, Antropov AS, Kivman GY, Kreuter J. Significant transport of doxorubicin into the brain with polysorbate 80-coated nanoparticles. *Pharm Res* 1999;16(10): 1564–1569. [PubMed: 10554098]

23. Siegal T, Horowitz A, Gabizon A. Doxorubicin encapsulated in sterically stabilized liposomes for the treatment of a brain tumor model: biodistribution and therapeutic efficacy. *J Neurosurg* 1995;83(6):1029–1037. [PubMed: 7490617]
24. Noguchi Y, Wu J, Duncan R, Strohalm J, Ulbrich K, Akaike T, et al. Early phase tumor accumulation of macromolecules: a great difference in clearance rate between tumor and normal tissues. *Jpn J Cancer Res* 1998;89(3):307–314. [PubMed: 9600125]
25. Maeda H, Wu J, Sawa T, Matsumura Y, Hori K. Tumor vascular permeability and the EPR effect in macromolecular therapeutics: a review. *J Control Release* 2000;65(1–2):271–284. [PubMed: 10699287]
26. Son YJ, Jang JS, Cho YW, Chung H, Park RW, Kwon IC, et al. Biodistribution and anti-tumor efficacy of doxorubicin loaded glycol-chitosan nanoaggregates by EPR effect. *J Control Release* 2003;91(1–2):135–145. [PubMed: 12932645]
27. Widder KJ, Morris RM, Poore GA, Howard DP, Senyei AE. Selective targeting of magnetic albumin microspheres containing low-dose doxorubicin: total remission in Yoshida sarcoma-bearing rats. *Eur J Cancer Clin Oncol* 1983;19(1):135–139. [PubMed: 6682771]
28. Pulfer SK, Ciccotto SL, Gallo JM. Distribution of small magnetic particles in brain tumor-bearing rats. *Journal of Neuro-Oncology* 1999;41:99–105. [PubMed: 10222429]
29. Leakakos T, Ji C, Lawson G, Peterson C, Goodwin S. Intravesical administration of doxorubicin to swine bladder using magnetically targeted carriers. *Cancer Chemother Pharmacol* 2003;51(6):445–450. [PubMed: 12802508]
30. Alexiou C, Jurgons R, Schmid RJ, Bergemann C, Henke J, Erhardt W, et al. Magnetic drug targeting--biodistribution of the magnetic carrier and the chemotherapeutic agent mitoxantrone after locoregional cancer treatment. *J Drug Target* 2003;11(3):139–149. [PubMed: 13129824]
31. Moffat BA, Reddy R, McConville P, Hall DE, Chenevert TL, Kopelman RR, et al. A novel polyacrylamide magnetic nanoparticle contrast agent for molecular imaging using MRI. *Molecular imaging* 2003;2(4):324–332. [PubMed: 14717331]
32. Reddy GR, Bhojani MS, McConville P, Moody J, Moffat BA, Hall DE, et al. Vascular targeted nanoparticles for imaging and treatment of brain tumors. *Clin Cancer Res* 2006;12(22):6677–6686. [PubMed: 17121886]
33. Wang YX, Hussain SM, Krestin GP. Superparamagnetic iron oxide contrast agents: physicochemical characteristics and applications in MR imaging. *Eur Radiol* 2001;11(11):2319–2331. [PubMed: 11702180]
34. Ross BD, Zhao Y-J, Neal ER, Stegman LD, Ercolani M, Ben-Yoseph O, et al. Contributions of cell kill and posttreatment tumor growth rates to the repopulation of intracerebral 9L tumors after chemotherapy: an MRI study. *Proc. Natl. Acad. Sci. USA* 1998;95:7012–7017. [PubMed: 9618530]
35. Lubbe AS, Alexiou C, Bergemann C. Clinical applications of magnetic drug targeting. *J Surg Res* 2001;95(2):200–206. [PubMed: 11162046]
36. Weissleder R, Bogdanov A, Neuwelt EA, Papisov M. Long-Circulating Iron-Oxides For Mr-Imaging. *Advanced Drug Delivery Reviews* 1995;16(2–3):321–334.
37. Jung CW, Jacobs P. Physical and chemical properties of superparamagnetic iron oxide MR contrast agents: ferumoxides, ferumoxtran, ferumoxsil. *Magn Reson Imaging* 1995;13(5):661–674. [PubMed: 8569441]
38. Pulfer SK, Gallo JM. Enhanced brain tumor selectivity of cationic magnetic polysaccharide microspheres. *J Drug Target* 1998;6(3):215–227. [PubMed: 9888308]
39. Ostergaard L. Principles of cerebral perfusion imaging by bolus tracking. *J Magn Reson Imaging* 2005;22(6):710–717. [PubMed: 16261573]
40. Simonsen CZ, Ostergaard L, Vestergaard-Poulsen P, Rohl L, Bjornerud A, Gyldensted C. CBF and CBV measurements by USPIO bolus tracking: reproducibility and comparison with Gd-based values. *J Magn Reson Imaging* 1999;9(2):342–347. [PubMed: 10077035]
41. Weisskoff RM, Zuo CS, Boxerman JL, Rosen BR. Microscopic susceptibility variation and transverse relaxation: theory and experiment. *Magn Reson Med* 1994;31(6):601–610. [PubMed: 8057812]
42. Lubbe AS, Bergemann C, Huhnt W, Fricke T, Riess H, Brock JW, et al. Preclinical experiences with magnetic drug targeting: tolerance and efficacy. *Cancer Res* 1996;56(20):4694–4701. [PubMed: 8840986]

43. Lubbe AS, Bergemann C, Riess H, Schriever F, Reichardt P, Possinger K, et al. Clinical experiences with magnetic drug targeting: a phase I study with 4'-epidoxorubicin in 14 patients with advanced solid tumors. *Cancer Res* 1996;56(20):4686–4693. [PubMed: 8840985]
44. Alexiou C, Arnold W, Klein RJ, Parak FG, Hulin P, Bergemann C, et al. Locoregional cancer treatment with magnetic drug targeting. *Cancer Res* 2000;60:6641–6648. [PubMed: 11118047]

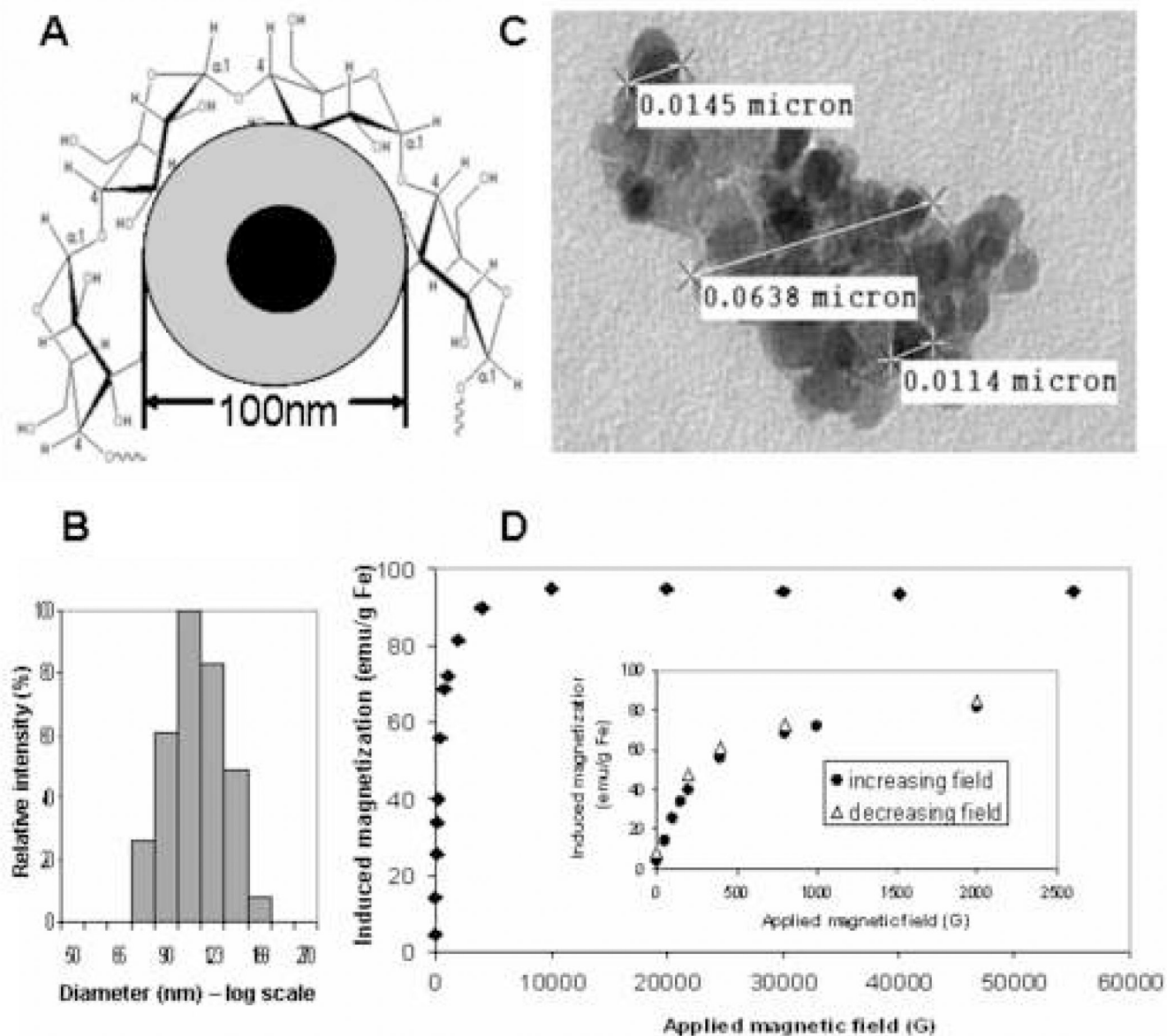


Figure 1. *In Vitro* characterization of magnetic nanoparticles. (A) Diagram of a magnetic nanoparticle consisting of magnetite (Fe_3O_4) core and a starch shell. (B) Intensity-weighted NICOMP particle size distribution of G100 colloid measured by Dynamic Light Scattering. (C) Typical TEM image of a single nanoparticle composed of multiple magnetite cores. (D) Magnetization curve of solid G100 at 293 K measured by SQUID exhibiting magnetic saturation (i.e. plateau at high magnetic field). The inset demonstrates negligible remanent magnetization indicative of superparamagnetic behavior.

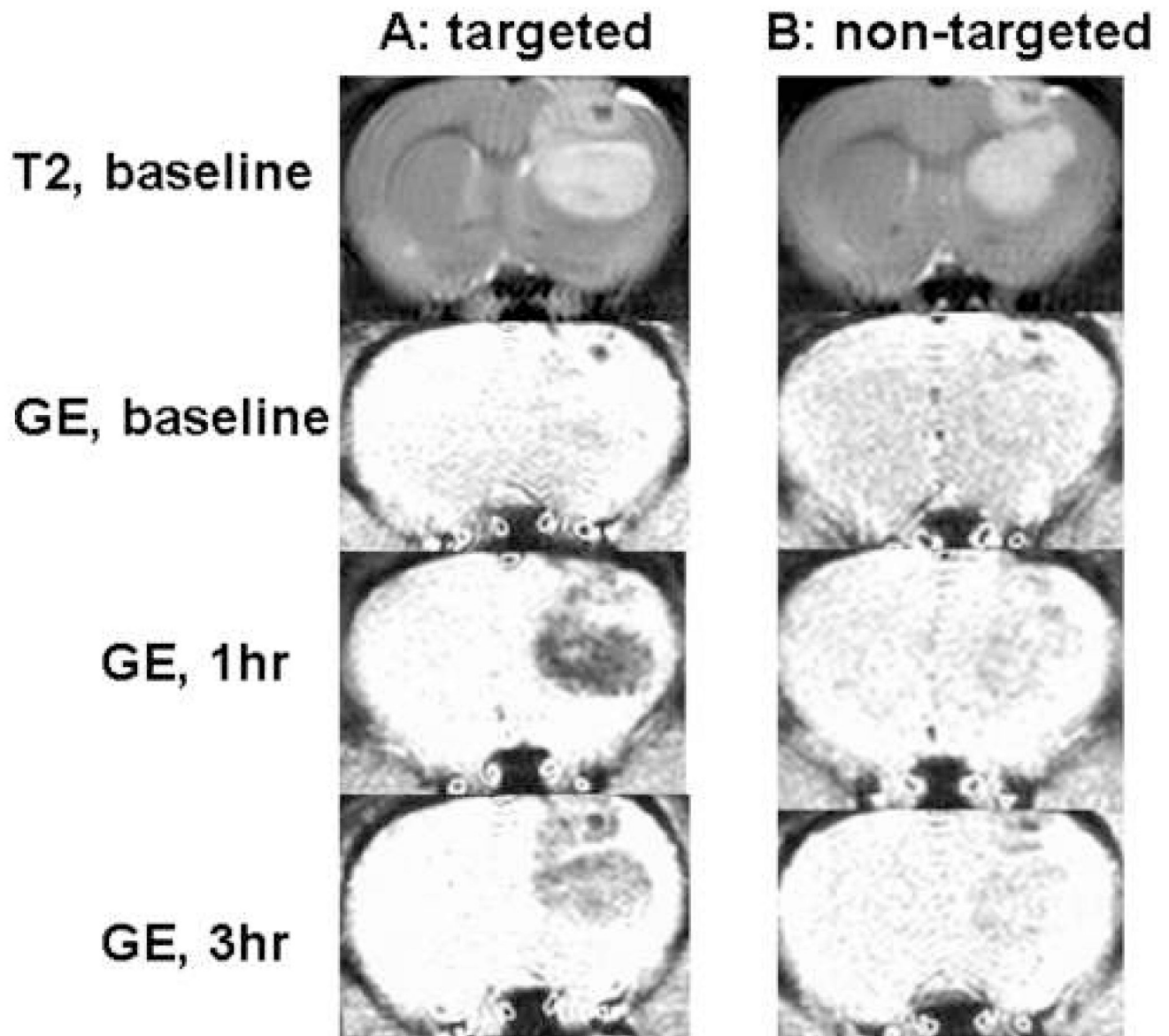


Figure 2. Representative subset of kinetic series of MRI scans demonstrating nanoparticle accumulation in 9L gliosarcoma (A) with and (B) without magnetic targeting. The spin echo T_2 -weighted baseline images illustrate the tumor location clearly observable as a hyper-intense lesion. GE baseline images were acquired before the nanoparticle injection, while 1-hr and 3-hr images were acquired 1 and 3 hours after nanoparticle administration, respectively.

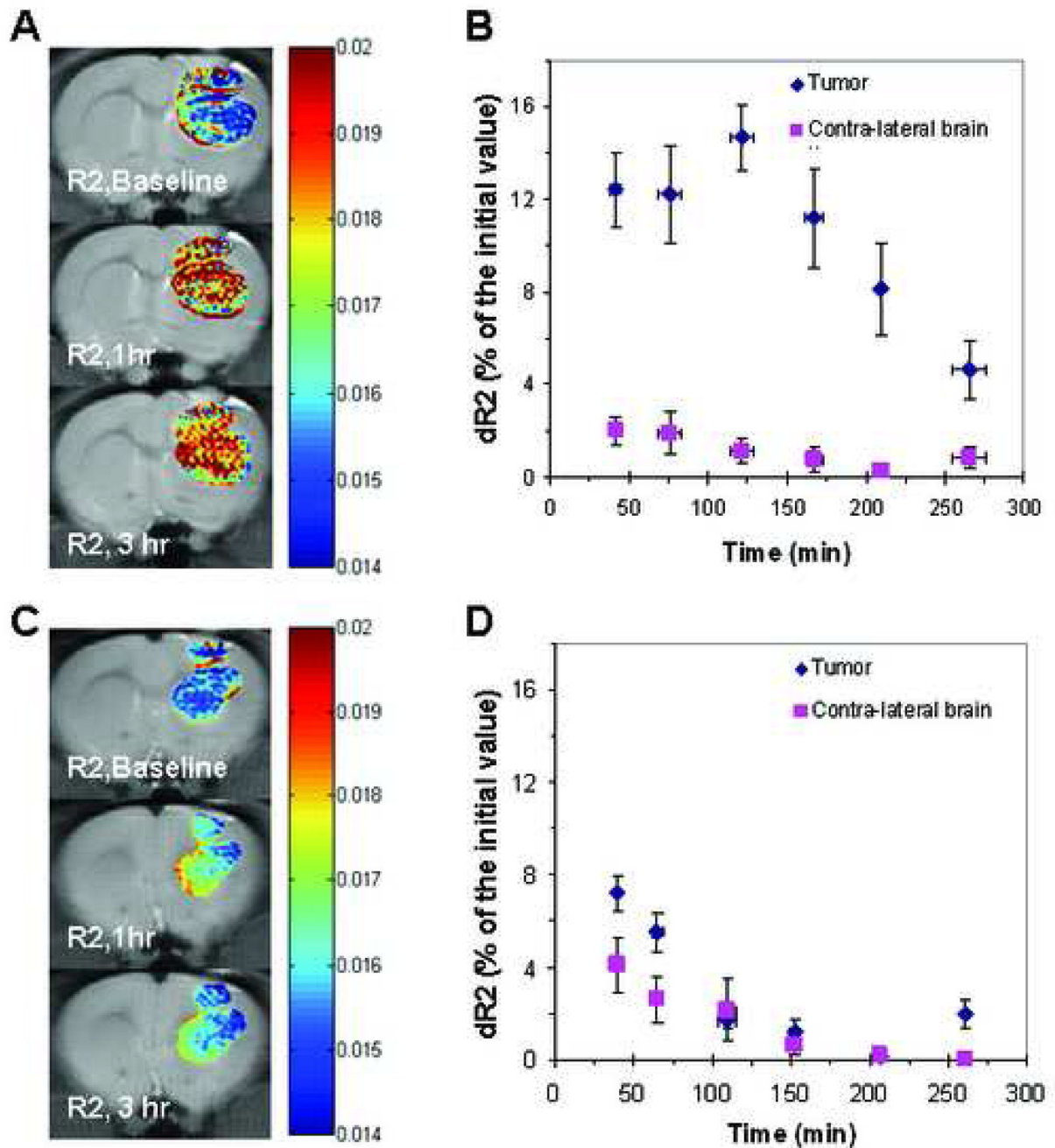


Figure 3. Kinetics of nanoparticle accumulation monitored by MRI in (A, B) targeted and (C, D) non-targeted groups of animals. (A, C) Representative series of R_2 maps (msec⁻¹) of the tumor tissue (color) superimposed onto the corresponding T2-weighted images acquired before (baseline) and 1–3 hours after nanoparticle administration in (A) targeted and (C) control rats. (B, D) Mean kinetic profiles of tumor and contra-lateral brain nanoparticle accumulation in (B) targeted and (D) control rats. Data expressed as MEAN \pm SE, n=5.

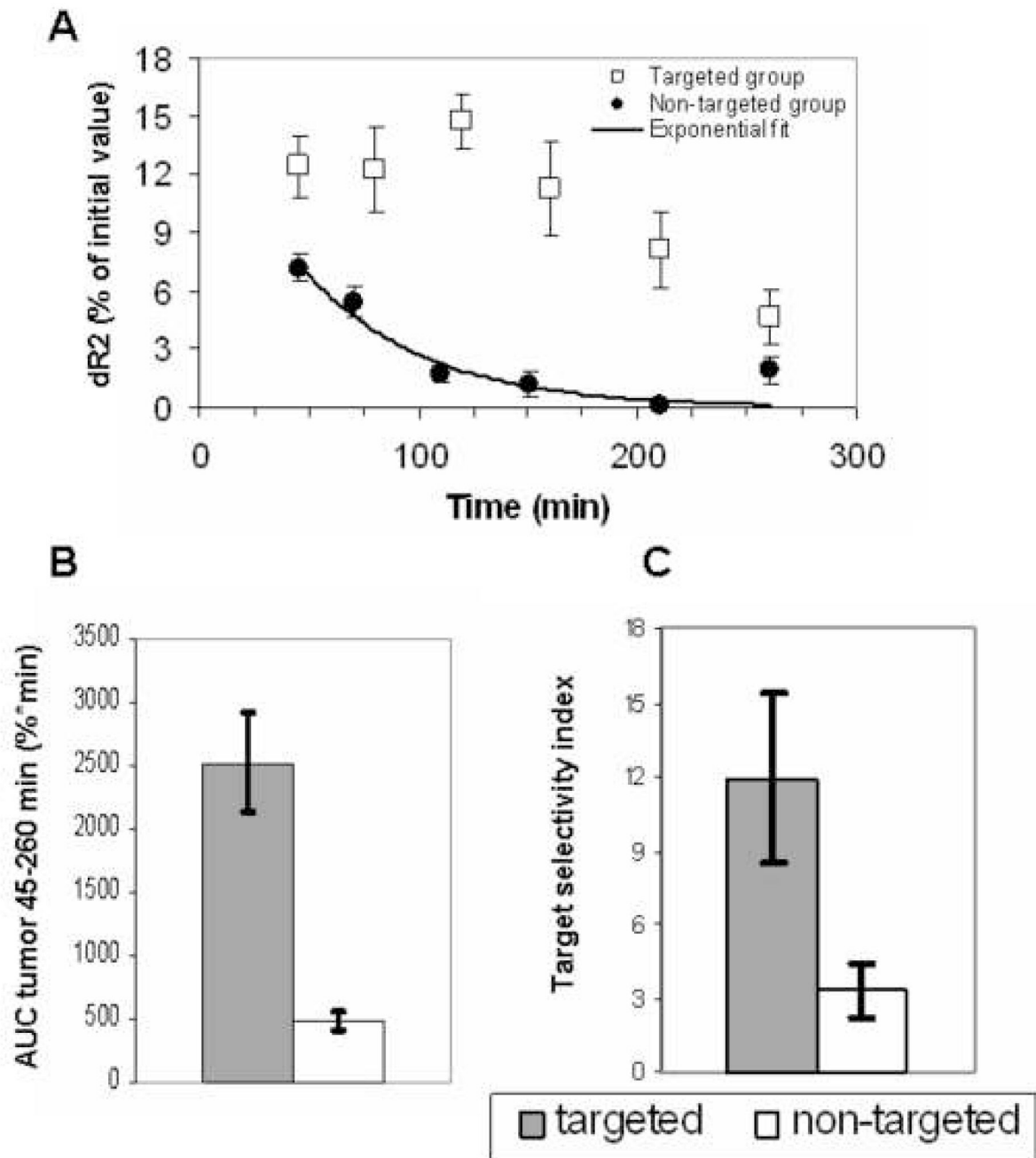


Figure 4.

Analysis of nanoparticle distribution in the brains of 9L gliosarcoma-bearing rats. (A) Mean kinetic profiles of nanoparticle accumulation in the tumor of the targeted and control rats. Data expressed as MEAN \pm SE, n=5. Exponential fit for the non-targeted group was calculated using nonlinear least squares regression method ($R^2=0.97$, RMSE=0.58). (B) Area under the dR₂-time curve of the tumor ROI over the interval of observation. The plot shows statistically significant difference between the targeted and the control groups ($p=0.005$). (C) Target selectivity index of nanoparticle accumulation in tumor versus contra-lateral brain ($p=0.025$).

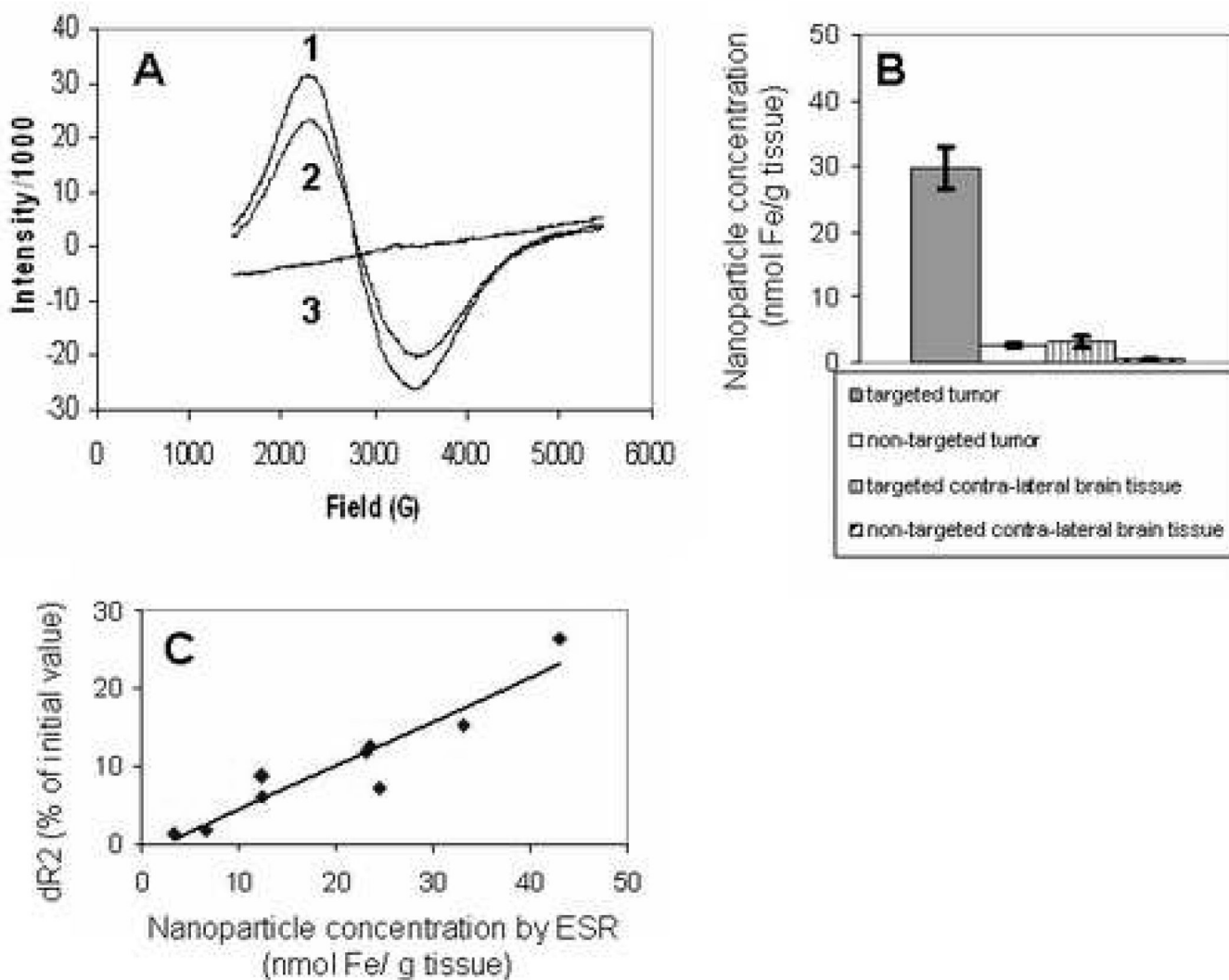


Figure 5. Analysis of nanoparticle concentration in excised animal tissues (glioma / contra-lateral brain) with ESR spectroscopy. (A) Typical ESR spectra of : #1- a standard solution of G100 magnetic nanoparticles; #2 – glioma of a rat injected with magnetic nanoparticles and subjected to *magnetic targeting*; #3 – glioma of a control rat not exposed to magnetic nanoparticles. (B) Nanoparticle concentration in excised tumor and contra-lateral brain tissues quantified by ESR spectroscopy. Data expressed as MEAN±SE, n=6. (C) A plot demonstrating linear correlation between the MRI-derived dR2 parameter and the ESR-determined nanoparticle concentration in excised tissue samples. ($R^2=0.88$, slope=0.57, $p=0.0001$)